A two-dimensional model of He/O_2 atmospheric pressure plasma needle discharge*

Qian Mu-Yang(钱沐杨)[a)†], Yang Cong-Ying(杨从影)[a)], Chen Xiao-Chang(陈小昌)[a)], Liu San-Qiu(刘三秋)[a)], Yan Wen(晏 雯)[b)], Liu Fu-Cheng(刘富成)[c)], and Wang De-Zhen(王德真)[b)]

[a)] *Department of Physics, Nanchang University, Nanchang* 330031, *China*
[b)] *School of Physics and Optoelectronic Technology, Dalian University of Technology, Dalian* 116023, *China*
[c)] *College of Physics Science and Technology, Hebei University, Baoding* 071002, *China*

(Received 27 May 2015; revised manuscript received 26 August 2015; published online 20 October 2015)

In this paper, a computational modeling study of stream propagation in the atmospheric-pressure helium plasma in ambient atmosphere (oxygen) is presented. A coupled fluid model between time-dependent plasma dynamics and steady state neutral gas flow is employed to provide a fundamental insight into the evolution of the streamers. The obtained simulation results showing that the sheath forms near the dielectric surface and shields the axial stream propagation. The stream front propagates with axial velocity in a range of 10^4 m/s–10^5 m/s. And, the increasing accumulated surface charge should be responsible for reducing the propagation velocity of the streamer front in the axial direction. Besides, when the gas flow rate is 1.1 standard liter per minute (SLM), we find that the concentration of oxygen drastically increases at a larger radial position near a treated surface. Therefore, Penning ionization by helium metastables and oxygen peaks at an off-axis position, corresponding to the ring-shaped emission profile in cylindrical coordinates. In this case, the simulated results show the ring-shaped ground atomic oxygen density profile near the treated surface ($z = 0.5$ mm) at a large gas flow rate of 1.1 SLM, which is consistent with the observation in a similar experiment.

Keywords: atmospheric pressure plasma needle discharge, streamer dynamics, cathode sheath

PACS: 52.65.Kj, 52.40.Kh, 52.25.Fi **DOI:** 10.1088/1674-1056/24/12/125203

1. Introduction

Non-thermal atmospheric pressure plasmas have recently received significant attention and have shown considerable promise in a wide range of practical applications such as biomedicine, nano-materials processing, and bacteria disinfection.[1–4] A number of different types of non-thermal atmospheric pressure plasma devices have been designed. Among them, the plasma needle is one of the most commonly applied plasma generators to produce homogenous microplasmas at the tip of the needle (on the order of few millimeters in diameter).[5] Helium is typically used as a source gas and fed through a dielectric tube with a velocity (about 10 m/s) into ambient air. The plasma is characterized by a fluid mechanical mixing layer where the source gas and air inter-diffuse. As the high-voltage sinusoidal or pulsed waveforms are applied to a needle-shaped electrode located inside a concentric gas-flow nozzle, the plasma discharge is localized to a region on the order of hundreds of micrometers to millimeters. When the plasma needle is applied to a surface, the jet of helium flow passes through the needle and impacts the surface in an open environment. Therefore, neutral gas flow should have an influence on the plasma needle discharge dynamics. We focus on the plasma needle discharge at atmospheric pressure.

Recently, the plasma needle has been studied for cell detachment, apoptosis in mammalian cells, and bacteria inactivation.[6,7] Goree *et al*.[8,9] reported that the killing pattern of *Streptococcus mutans* bacteria varied from a circle to an annular ring as the feed gas flow rate is increased, depending on the input power. Therefore, several other researchers have addressed the influences of neutral gas flow on non-thermal atmospheric pressure plasma and try to explain the ring-shaped emission patter and associated bacteria killing pattern observed by Goree *et al*. Sakiyama and Graves[10] demonstrated that the "ion wind" and gas heating have only minor effects on He/N_2 atmospheric pressure plasma needle discharge, and ambient N_2 diffusion against the convective helium flow should be responsible for the unique ring-shaped light emission. As is well known, atomic oxygen is antibacterial.[11] Therefore, they reported the gas flow dependence of ground state atomic oxygen near the treated surface by using two-photo absorption laser-induced fluorescence (TALIF) spectroscopy, and the results indicated that the bacteria killing ring-shaped pattern was due to the ground state atomic oxygen.[12] In more detail, a circular density distribution was observed at 0.5 SLM, whereas the profile turned to a ring at 1.0 SLM. Besides, Yan *et al*.[13]

*Project supported by the National Natural Science Foundation of China (Grant No. 11465013), the International Science and Technology Cooperation Program of China (Grant No. 2015DFA61800), and the Natural Science Foundation of Jiangxi Province, China (Grant No. 20151BAB212012).

†Corresponding author. E-mail: qianmuyang@ncu.edu.cn

© 2015 Chinese Physical Society and IOP Publishing Ltd

investigated the effect of the needle electrode on the plasma jet characteristics, and the simulation results indicate that the needle electrode has an evident influence on the plasma jet characteristics.

Several issues that still need to be addressed include the investigation of the underlying physical mechanisms that dominate the unique ring-shaped bacteria killing pattern and the two distinct ground atomic oxygen profiles depending on the gas flow rate. Our primary concern in this paper is therefore to model He/O_2 atmospheric pressure plasma needle discharge and try to reproduce the ring-shaped ground state atomic oxygen density profile near the treated surface. The first step of the study is to establish a two-dimensional self-consistent fluid model, in which electrohydrodynamic force, plasma joule heating and photo-ionization mechanism are not considered, and background pre-ionization is assumed instead. The initial electron and ion densities in the gas are considered to be 10^7 cm^{-3} and uniformly distributed. Only a single streamer is studied in our case, which is valid when the frequency of the voltage pulse is sufficiently low. Otherwise, the accumulation of active species takes place and the Penning effect (i.e. long-lifetime helium metastables) arising from preceding discharges cannot be neglected.[14,15] Besides, the 'air' in the current model is assumed to be pure O_2, partly due to computational limitations. The streamer characteristic parameters and cathode sheath are also studied.

2. Model description

Our model consists of a coupled set of models: a neutral gas fluid model and a plasma dynamics model in two-dimensional cylindrical coordinates. More specially, steady state equations are solved for neutral gas flow, whereas we solve time-dependent equations for plasma discharge. The schematic diagram of the needle discharge with a treated surface is shown in Fig. 1. The needle is indicated by the points *A*, *B*, and *C* in Fig. 1, its tip is shaped as a semi-sphere with a radius 0.2 mm, and its total length is 2.5 mm. The needle is concentric with an insulator indicated by points *D*, *E*, and *F*, which has a radius of 1 mm. The dielectric constant of the insulator is $5\varepsilon_0$ where ε_0 is the vacuum permittivity. The edges of the insulator tube are rounded with a curvature radius of 50 μm (point *E* in Fig. 1). The needle tip is flush with the end of the tube. A treated surface is simplified into a planar quartz plate (marked by points *G*, *H*, *I*, and *J* in Fig. 1). The gap distance between the needle tip and the treated surface is 2.5 mm. The thickness of the quartz plate is 0.2 mm with relative permittivity 5 unless otherwise stated. The electrical potential is zero at the backside of the quartz plate (indicated by points *I* and *J* in Fig. 1), where a grounded metal plate is assumed to be attached. A 4.5-kV positive voltage is applied to the needle tip as can be seen in Fig. 1. Besides, an external *RC* ($R = 3$ kΩ, $C = 2$ pF) network is added to the plasma discharge circuit, which is used to prevent the discharge from arcing. The voltage is assumed to be a square wave 'pulse', i.e., the peak voltage is applied instantaneously at the beginning of the simulation and remains constant for the simulation duration ($t = 0$ point indicates the beginning of the simulation). The source gas consists of He with O_2 as an impurity at a mole fraction of 0.005 and flows into the domain from the boundary between the needle and the insulate tube (as indicated by points *C* and *D* in Fig. 1). The gas flow rate considered in the simulation is 1.1 SLM.

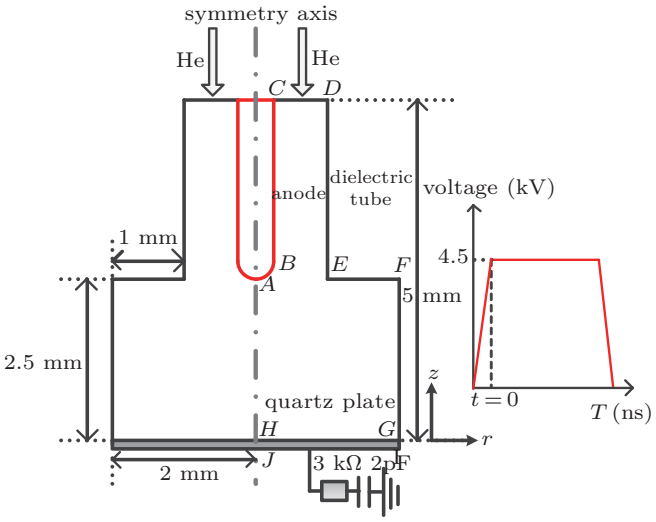


Fig. 1. (color online) Side view schematic diagram of the discharge setup and the simulation domain.

The governing equations for the neutral gas model consist of the total mass continuity equation, Navier–Stokes equation, and the mass continuity equation for O_2 and the ideal gas law as follows:

$$\nabla \cdot (\rho \boldsymbol{u}) = 0, \tag{1}$$

$$[\rho \boldsymbol{u} \cdot \nabla \boldsymbol{u}] = -\nabla p - [\nabla \cdot \tau] - \boldsymbol{F}, \tag{2}$$

$$\nabla \cdot (\rho \omega_{\mathrm{O}} \boldsymbol{u} - \rho D_{\mathrm{g}} \nabla \omega_{\mathrm{O}}) = 0, \tag{3}$$

$$p = \sum_i n_i k T_{\mathrm{g}}, \tag{4}$$

where $\boldsymbol{u}$ is the mass-averaged velocity vector, ρ is the total density, p is the pressure, τ is the stress tensor of Newtonian fluid, $\boldsymbol{F}$ is the body force field (buoyancy), ω_{O} is the mass fraction of dry oxygen, D_{g} is the binary diffusion coefficient, and T_{g} is the gas temperature 300 K. Subscript i in Eq. (4) represents the species of gases (i.e., He and O_2). The density in Eq. (4) is calculated from mass fraction by $n_i = \rho \omega_i / m_i$, where m_i is the mass of species i. The source gas flow rate considered in the simulation is 1.1 SLM. The pressure at the exit is fixed to be 1 atm (1 atm = 1.01325×10^5 Pa) and the gas temperature is 300 K. The boundary conditions are summarized in Table 1.

Table 1. Boundary conditions for the neutral gas model. The symbols (*A*–*J*) correspond to the vertexes in Fig. 1. u_r and u_z are r and z components of the velocity field, respectively. $\boldsymbol{n}$ is the normal vector to the boundary.

	u_r	u_z	$\omega_{\rm O}$
AH	$u_r = 0$	$\dfrac{\partial u_r}{\partial z} = 0$	$\dfrac{\partial \omega_{\rm O}}{\partial r} = 0$
ABC	$u_r = 0$	$u_z = 0$	$\nabla\omega_{\rm O}\cdot\boldsymbol{n} = 0$
CD	$u_r = 0$	$u_z = u_0^{\rm a}$	$\omega_{\rm O} = 3.8\times10^{-2{\rm c}}$
DEF	$u_r = 0$	$u_z = 0$	$\nabla\omega_{\rm O}\cdot\boldsymbol{n} = 0$
FG	$\left(\dfrac{\partial u_r}{\partial r}\right) - \dfrac{1}{3}(\nabla\cdot\boldsymbol{u}) = 0^{\rm b}$	$u_z = 0$	$\omega_{\rm O} = 1.0$
GH	$u_r = 0$	$u_z = 0$	$\partial\omega_{\rm O}/\partial z = 0$

[a]Deduced from the helium gas flow rate. [b]Corresponds to zero stress tensor. [c]Deduced from the mole fraction of O_2 in the source gas (0.005).

The plasma dynamics model is based on the classical fluid model, which is governed by the continuity equations in the drift-diffusion approximation, the electron energy conservation, and Poisson's equation, which are given as follows:

$$\frac{\partial n_i}{\partial t} + \nabla\cdot\Gamma_i = \sum_j R_{ij} = S_i, \tag{5}$$

$$\Gamma_i = \mathrm{sgn}(q_i)n_i\mu_i\boldsymbol{E} - D_i\nabla n_i + n_i\boldsymbol{u}, \tag{6}$$

$$\frac{\partial(n_{\rm e}\varepsilon)}{\partial t} + \nabla\cdot\left(\frac{5}{3}\varepsilon\Gamma_{\rm e} - \frac{5}{3}n_{\rm e}D_{\rm e}\nabla\varepsilon\right) = -e\Gamma_{\rm e}\cdot\boldsymbol{E} - \sum_j \Delta E_j K_{{\rm inel},j} - 3\frac{m_{\rm e}}{m_{\rm He}}K_{\rm el}k_{\rm b}(T_{\rm e}-T_{\rm g}), \tag{7}$$

$$-\varepsilon_0\nabla^2\phi = \varepsilon_0\nabla\cdot\boldsymbol{E} = \sum_j q_j n_j, \tag{8}$$

where subscript i, e, and He indicate the i-th species, electrons, and helium gas, respectively, Γ is the flux in the drift-diffusion approximation, R_{ij} is the j-th reaction rate shown in Table 3, q is the charge, μ is the mobility, $\boldsymbol{E}$ is the electric field, ϕ is the potential and ε is the mean electron energy, ΔE and $K_{\rm inel}$ are the energy loss to inelastic collisions and the corresponding reaction rate, respectively, and ε_0 is the vacuum permittivity.

The boundary conditions for the particle flux at the needle, the insulator, and the treated surface are given as follows:

$$\Gamma_{\rm e}\cdot\boldsymbol{n} = \frac{1}{4}n_{\rm e}\sqrt{8k_{\rm b}T_{\rm e}/\pi m_{\rm e}} - \alpha_{\rm s}\sum_i\gamma_i(\Gamma_{\rm i}\cdot\boldsymbol{n}) + \alpha_{\rm s}'\mu_{\rm e}n_{\rm e}\boldsymbol{E}, \tag{9}$$

$$\Gamma_{\rm i}\cdot\boldsymbol{n} = \frac{1}{4}n_{\rm i}\sqrt{8k_{\rm b}T_{\rm i}/\pi m_{\rm i}} - \alpha_{\rm s}'\mu_{\rm i}n_{\rm i}\boldsymbol{E}, \tag{10}$$

$$\Gamma_{\rm m}\cdot\boldsymbol{n} = \frac{1}{4}n_{\rm m}\sqrt{8k_{\rm b}T_{\rm g}/\pi m_{\rm m}}, \tag{11}$$

$$\Gamma_{\varepsilon}\cdot\boldsymbol{n} = \frac{1}{2}n_{\varepsilon}\sqrt{8k_{\rm b}T_{\rm e}/\pi m_{\rm e}} - \alpha_{\rm s}2k_{\rm b}T_{\rm e}\sum_i\gamma_i(\Gamma_{\rm i}\cdot\boldsymbol{n}). \tag{12}$$

where e, i, m, and ε denote the electron, ion, metastable, and electron energy, respectively; $T_{\rm i}$ and $T_{\rm g}$ are the ion and background gas temperature ($T_{\rm i} = T_{\rm g} = 300$ K in this paper); $\boldsymbol{n}$ is the normal vector pointing toward the surface; γ is the second electron emission probability. The secondary electron coefficient is 0.05 in this model. The surface charge accumulation is considered on the dielectric surface. $\alpha_{\rm s}$ and $\alpha_{\rm s}'$ are switching functions depending on the inner product of $\boldsymbol{E}$ and $\boldsymbol{n}$. The self-bias potential at the surface of the quartz plate is calculated from Gauss's law:

$$(\boldsymbol{D}_2 - \boldsymbol{D}_1)\cdot\boldsymbol{n} = \sigma_{\rm s}, \quad \frac{{\rm d}\sigma_{\rm s}}{{\rm d}t} = \boldsymbol{J}_i\cdot\boldsymbol{n} + \boldsymbol{J}_{\rm e}\cdot\boldsymbol{n}, \tag{13}$$

where $\boldsymbol{D}_1$ and $\boldsymbol{D}_2$ are the electric displacement on the two sides of the dielectric surface, $\boldsymbol{J}_{\rm i}\cdot\boldsymbol{n}$ and $\boldsymbol{J}_{\rm e}\cdot\boldsymbol{n}$ are the normal component of the total ion current density and total electron current density on the cathode surface, respectively, $\sigma_{\rm s}$ is the net surface charge accumulated on the dielectric surface. The boundary conditions are summarized in Table 2.

Table 2. Boundary conditions for the plasma dynamics model. The symbols (*A*–*J*) correspond to the vertexes in Fig. 1. Subscripts e, i, and m denote the electron, ions, and metastables, respectively.

	$n_{\rm e}$	$n_{\rm i}$	$n_{\rm m}$	n_ε	ϕ
ABC	Eq. (9)	Eq. (10)	equation (11)	Eq. (12)	4.5 kV
AH	$\dfrac{\partial n_{\rm e}}{\partial r} = 0$	$\dfrac{\partial n_{\rm i}}{\partial r} = 0$	$\dfrac{\partial n_{\rm m}}{\partial r} = 0$	$\dfrac{\partial n_\varepsilon}{\partial r} = 0$	$\dfrac{\partial \phi}{\partial r} = 0$
CD	$\dfrac{\partial n_{\rm e}}{\partial z} = 0$	$\dfrac{\partial n_{\rm i}}{\partial z} = 0$	$\dfrac{\partial n_{\rm m}}{\partial z} = 0$	$\dfrac{\partial n_\varepsilon}{\partial z} = 0$	$\dfrac{\partial \phi}{\partial z} = 0$
DEF	Eq. (9)	Eq. (10)	Eq. (11)	Eq. (12)	$\varepsilon_0\nabla\phi = \sigma_{\rm s}$
FG	$\dfrac{\partial n_{\rm e}}{\partial r} = 0$	$\dfrac{\partial n_{\rm i}}{\partial r} = 0$	$\dfrac{\partial n_{\rm m}}{\partial r} = 0$	$\dfrac{\partial n_\varepsilon}{\partial r} = 0$	$\dfrac{\partial \phi}{\partial r} = 0$
GH	Eq. (9)	Eq. (10)	Eq. (11)	Eq. (12)	Eq. (13)

The plasma chemistry considered in this model consists of 13 species and 37 reactions shown in Table 3. The species considered in this model are e, He, He^+, He_2^+, He^*, He_2^*, O_2, O_2 (V), O_2 (R), O_2^-, O_2^+, O_2^*, O. For reactions which produce O_2 in different rotational and vibrational states, their reaction rates are calculated by cross section data from Bolsig+.[16] The helium and helium–oxygen chemistry reaction sub-mechanisms are cited from Refs. [17] and [18], and the oxygen chemistry sub-mechanisms are cited from Ref. [17].

Table 3. Helium–oxygen chemistry reactions used in this study.

Helium–oxygen chemistry (molecules–meters–electron volt)						
Rxn	Reaction	A	B	C	Activation energy	Ref.
Helium chemistry						
R1	$e + He \rightarrow e + He$		BOLSIG		0	[16]
R2	$e + He \rightarrow e + He^*$		BOLSIG+		19.8	[16]
R3	$e + He \rightarrow 2e + He^+$		BOLSIG+		24.6	[16]
R4	$e + He^* \rightarrow 2e + He^+$	4.661×10^{-16}	0.6	4.78	4.78	[17]
R5	$2He^* \rightarrow e + He^+ + He$	4.5×10^{-16}	0	0	–15.0	[17]
R6	$e + 2He^+ \rightarrow He + He^*$	5.386×10^{-13}	–0.5	0	0	[17]

Table 3. (*Continued*).

Helium–oxygen chemistry (molecules–meters–electron volt)						
Rxn	Reaction	A	B	C	Activation energy	Ref.
Helium chemistry						
R7	$He^* + 2He \rightarrow He + He_2^*$	1.3×10^{-45}	0	0	0	[17]
R8	$He^* + 2He \rightarrow He + He_2^+$	1.0×10^{-43}	0	0	0	[17]
R9	$e + He^+ \rightarrow He^*$	6.76×10^{-19}	–0.5	0	0	[17]
R10	$e + He^* \rightarrow e + He$	2.0×10^{-16}	0	0	0	[17]
R11	$2e + He^+ \rightarrow e + He^*$	6.186×10^{-39}	–4.4	0	0	[17]
R12	$e + He^+ + He \rightarrow He + He^*$	6.66×10^{-42}	–2	0	0	[17]
R13	$2e + He_2^+ \rightarrow e + He_2^*$	2.8×10^{-32}	0	0	0	[17]
R14	$e + He_2^+ + He \rightarrow 2He + He^*$	3.5×10^{-39}	0	0	0	[17]
R15	$e + He_2^+ + He \rightarrow He + He_2^*$	1.5×10^{-39}	0	0	0	[17]
R16	$2e + He_2^+ \rightarrow e + He^* + He$	2.8×10^{-32}	0	0	0	[17]
Oxygen chemistry						
R17	$e + O_2 \rightarrow e + O_2$ (VIB3v1)		BOLSIG+		0.579	[16]
R18	$e + O_2 \rightarrow e + O_2$ (VIB4v1)		BOLSIG+		0.772	[16]
R19	$e + O_2 \rightarrow e + O_2$ (A1)		BOLSIG+		0.977	[16]
R20	$e + O_2$ (A1)$\rightarrow e + O_2$		BOLSIG+		–0.977	[16]
R21	$e + O_2 \rightarrow e + O_2$ (B1)		BOLSIG+		1.627	[16]
R22	$e + O_2$ (B1)$\rightarrow e + O_2$		BOLSIG+		–1.627	[16]
R23	$e + O_2 \rightarrow e + O_2$ (EXC)		BOLSIG+		4.5	[16]
R24	$e + O_2$ (EXC)$\rightarrow e + O_2$		BOLSIG+		–4.5	[16]
R25	$e + O_2 \rightarrow O + O^-$		BOLSIG+		3.6	[16]
R26	$e + O_2 \rightarrow e + 2O$		BOLSIG+		3.58	[16]
R27	$e + O_2 \rightarrow e + O + O$ (1D)		BOLSIG+		8.4	[16]
R28	$e + O_2 \rightarrow 2e + O_2^+$		BOLSIG+		12.06	[16]
R29	$O^- + O_2^+ \rightarrow O + O_2$	3.464×10^{-12}	–0.5	0	0	[18]
R30	$e + 2O_2 \rightarrow O_2 + O_2^-$	5.17×10^{-43}	–1	0	0	[18]
R31	$O_2^+ + O_2^- \rightarrow 2O_2$	2×10^{-13}	0	0	0	[18]
R32	$O_2^+ + O_2^- + M \rightarrow 2O_2 + M$	2×10^{-37}	0	0	0	[17]
R33	$O^- + O \rightarrow O_2 + e$	5×10^{-13}	0	0	0	[17]
R34	$O^- + O_2^+ \rightarrow 3O$	1×10^{-13}	0	0	0	[17]
Helium–oxygen interactions						
R35	$O_2^- + He_2^+ \rightarrow 2He + O_2$	1.0×10^{-13}	0	0	0	[17]
R36	$He^* + O_2 \rightarrow He + O_2^+ + e$	2.6×10^{-16}	0	0	0	[17]
R37	$He_2^* + O_2 \rightarrow 2He + O_2^+ + e$	2.6×10^{-16}	0	0	0	[17]

Note: (i) Species 'M' in reactions R32 represents the third-body species (He, O_2, and N_2). (ii) The tabulated reaction rates are given in the Arrhenius form. (iii) Units: Two-body reaction rate coefficient ($m^3\cdot s^{-1}$). Three-body reaction rate coefficient ($m^6\cdot s^{-1}$). Electron temperature T_e (eV). Gas (heavy particle) temperature T_g (K).

All governing equations are solved by COMSOL with the finite element method. First, we solve Eqs. (1)–(4) in order to obtain a steady state fluid flow field of the neutral gas. Then the flow field results are coupled to the time-dependent solver, which is used to solve the plasma dynamic equations (5)–(8). The free triangle mesh method is used to discretize the governing equations. Close to the needle tip and the treated surface, the minimum mesh size is 1 μm. The mesh resolution must be high enough to describe the complicated chemical reactions in the sheath. The complete mesh consists of 167847 cells, and the total number of degrees of freedom is about 1.27×10^6.

3. Results and discussion

3.1. Neutral gas fluid properties

Figures 2(a) and 2(b) show the profiles of oxygen mole fraction and magnitude of velocity, respectively. The source gas flows downward along the channel between the needle and the insulator tube from the inlet ($z = 5$ mm) to the treated surface ($z = 0$ mm). According to previous study,[10] the needle plasma discharge is restricted to the domain ($r < 2$ mm). Thus, in our work, we take radial length $r = 2$ mm. As is well known, the gas concentration profile is mostly determined by a balance between the convective flow of the source gas and backdiffusion of ambient air (oxygen) from the surroundings, besides being in the vicinity of the needle tip. In our work, the source gas flow rate is 1.1 SLM, which is equal to a mean inlet velocity of about 6 m/s. As can be seen in Fig. 2, the needle tip is almost entirely surrounded by the source gas, which is due to the fact that the convective flow is dominant against backdiffusion of O_2 at a smaller radial domain. Besides, the fluid velocity becomes mostly radial near the stagnation point at the plate surface. However, a considerable increase in O_2 concentration is observed at larger radial positions since the gas velocity decreases with radius. In other words, the backdiffusion against the convective transport is more prominent at a larger radial position, which coincides with the result reported by Sakiyama and Graves,[10] and Sakiyama.[12]

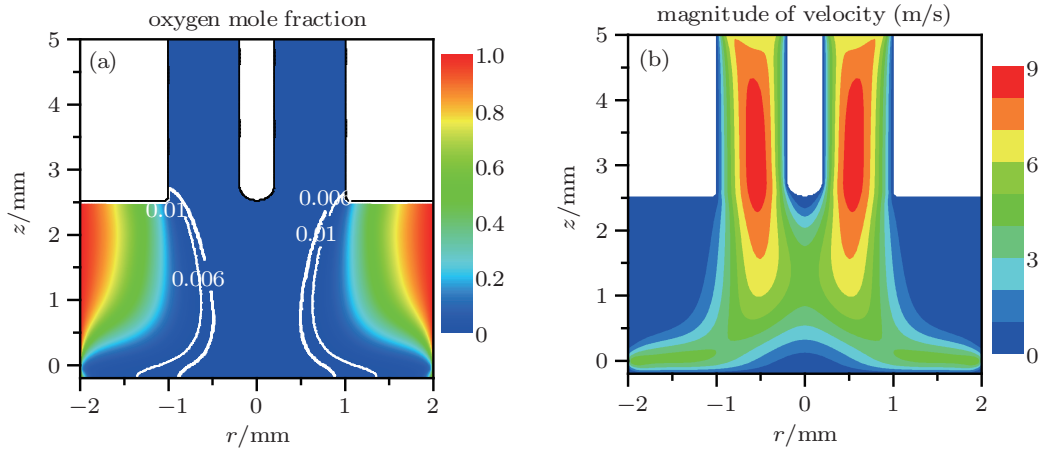
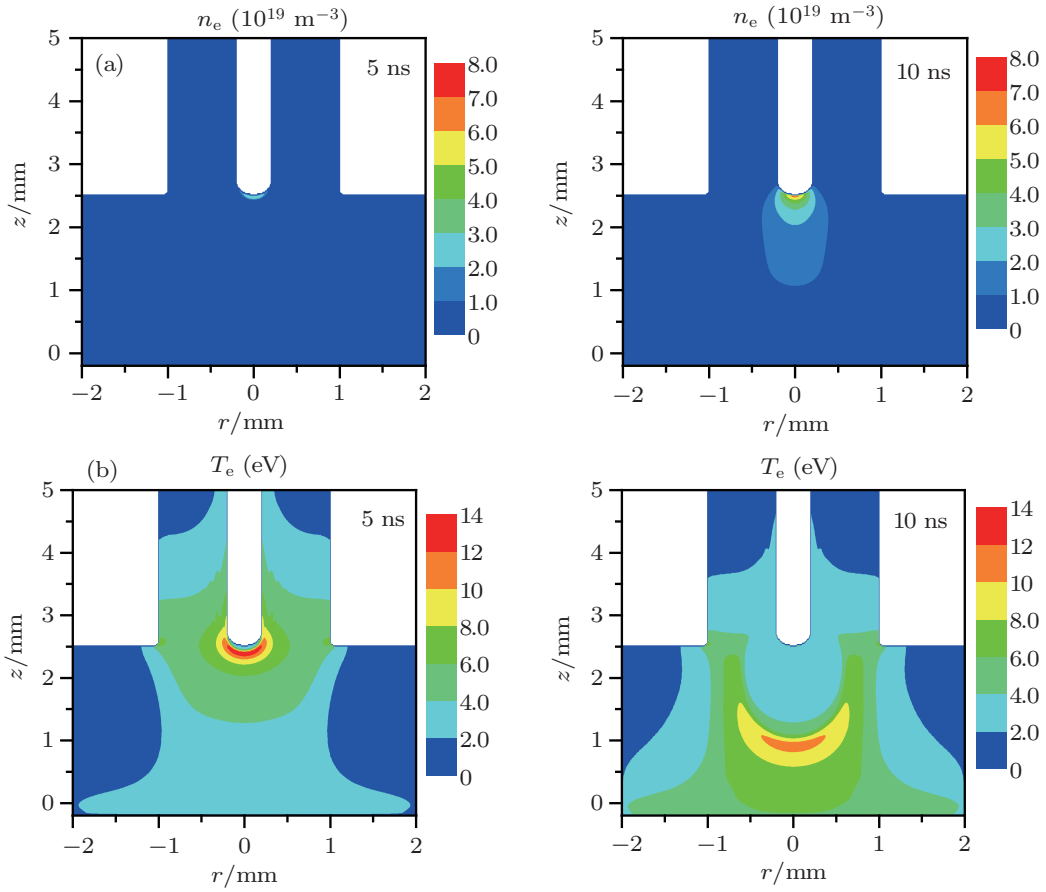


Fig. 2. (color online) (a) Mole fraction of oxygen and (b) magnitude of velocity distribution.

3.2. Discharge characteristics

The evolutions of typical plasma characteristic parameters (electron density, electron temperature, space charge density, and electric field profile) are shown in Fig. 3. For a given applied voltage (4.5 kV), the needle plasma discharge occurs near the needle tip. In the first 5 ns, the discharge takes place at the near needle tip position, which is due to the strong electric field produced by the small radius of curvature (0.2 mm). From 3 ns to 14 ns, the streamer propagates along the axial and toward the treated surface under the external and self-generated electric field. As shown in Fig. 3(a), the discharge region expands simultaneously toward radial and axial directions, which was not observed in our previous model with the uniform He concentration profile.[19] The peak electron temperature mainly concentrates on the head of the streamer as shown in Fig. 3(b). As a given positive pulse is applied, the positive space charges with a density of 10^{18} e/m^3 are concentrated at the head and the radial boundaries of the streamer as shown in Fig. 3(c). As can be seen in Figs. 3(c) and 3(d), the larger space charges in the stream front create an enhanced electric field, causing an electron avalanch, resulting in the propagating ionization wave. Thus, the peaks of electric field and electron impact ionization rate are located on the head of the streamer.



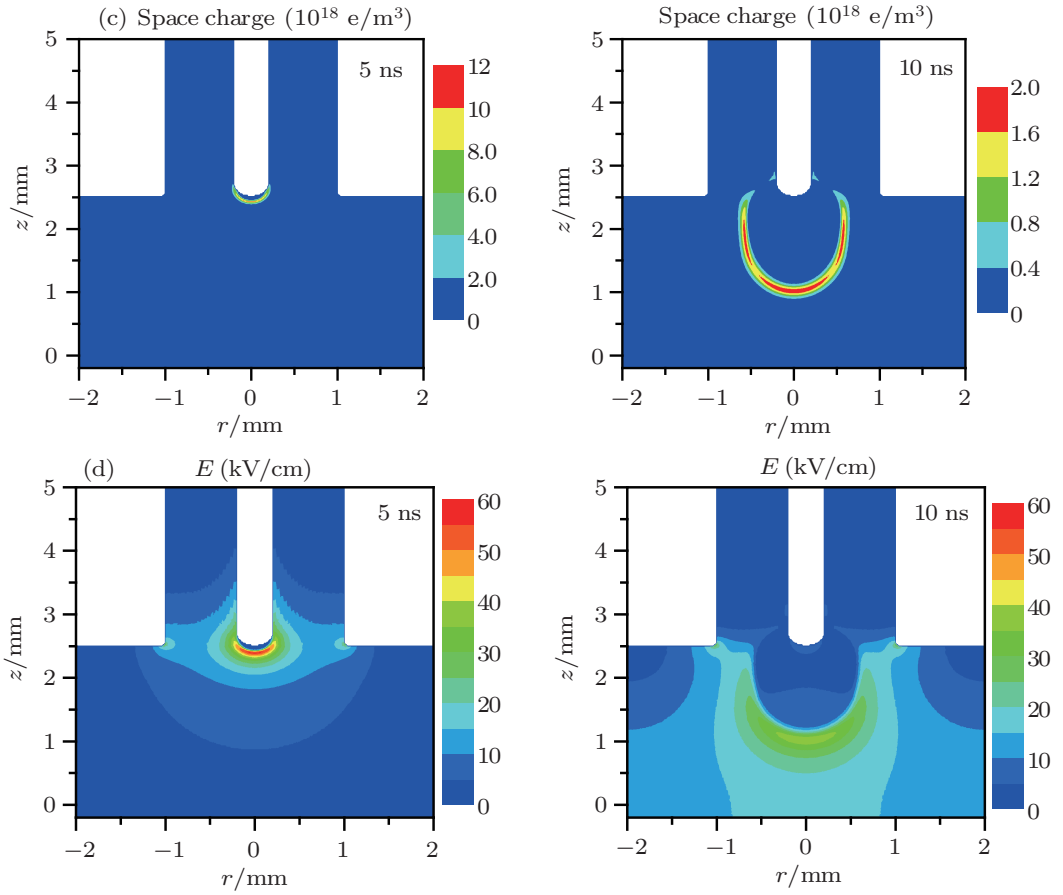


Fig. 3. (color online) Typical streamer propagations at 5, 10 ns after the start of the 4.5 kV pulse. (a) Electron density, (b) electron temperature, (c) positive space charge density, and (d) electric field.

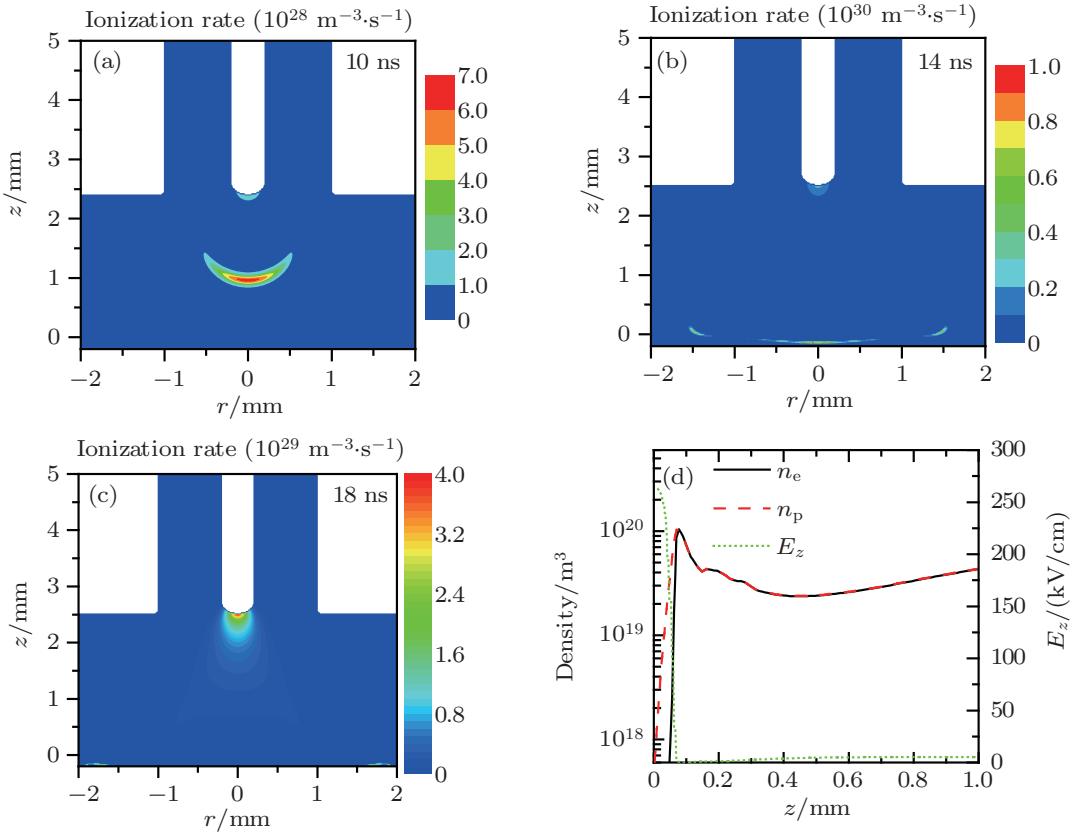


Fig. 4. (color online) Total ionization rates (including R3–R5, R28, R36, and R37) of needle plasma at (a) 10 ns, (b) 14 ns, (c) 18 ns, and (d) the axial profiles of electron and positive ion densities, and the electric fields in the vicinity of the sheath at 14 ns.

The ionization rate is used to predict the streamer propagation.[17,20] Therefore, figure 4 shows the total ionization rates (including ionizations of He and O_2) at 10 ns, 14 ns, and 18 ns, respectively. As can be seen in Fig. 4(b), the streamer front reaches the treated surface, and a cathode sheath is thus formed in the vicinity of the surface. In the first 14 ns, the total ionization rate is mostly concentrated in the streamer head with less ionization distributed near the needle tip. Besides, it is clearly seen in Figs. 4(a) and 4(b) that the peak ionization is located at the axis in the streamer head in our case. It is interesting to notice that a significant increase in ionization rate is observed at a larger radial position ($r = 1.6$ mm), which is due to the fact that backdiffusion against the convective transport is more prominent at larger radial positions. From 13 ns to 15 ns, due to the secondary electron emission process which can provide seed electrons ahead of the streamer front, the streamer front moves towards the cathode again. After that, the streamer front spreads along the dielectric surface as shown in Fig. 4(c). In other words, the dielectric coated ground electrode is found to terminate the streamer with a spread-out plasma root, which is similar to the experimental result.[21] Figure 4(d) shows the profiles of axial electron and positive ion densities, and the electric field in the vicinity of the sheath, which presents the typical cathode sheath structure at 14 ns. As can be seen, the sheath thickness is about 0.05 mm, and the peak z component of electric field reaches 265 kV/cm on the cathode.

The axial velocity of the streamer front as a function of time in the first 14 ns is shown in Fig. 5(a). It can be seen that the streamer front will start to be accelerated as soon as it is launched from the needle tip. At 11 ns, it reaches its maximum velocity 5.25×10^5 m/s and then drops rapidly. These are similar to experimental observations.[22,23] As discussed in Fig. 4(d), a cathode sheath is formed in the vicinity of the treated surface, which is responsible for the deceleration of streamer propagation. Figure 5(b) shows the temporal variations of cathode sheath thickness at $r = 0$ mm radial position. From 13 ns to 15 ns, it is clearly observed that due to the secondary electron emission process, the sheath thickness is reduced to a minimum of 0.01 mm. Then, the sheath thickness has a slight increase before stabilizing at 0.02 nm. In order to address why the streamer front terminates at the treated surface with a spread-out plasma root, figure 6 shows the temporal evolutions of the radial distributions of surface charge density on the treated surface. As can be seen from 14 ns to 17 ns, the positive surface charge density peaks appear on the symmetric axis and gradually decrease away from the axis, and its peak value increases from 0.07 nC/cm^2 to 42 nC/cm^2. From 18 ns to 22 ns, the positive surface charge density increases further and distributes along the entire dielectric surface. As is well known, the higher the surface charge density accumulated on the dielectric surface is, the stronger the feedback electric field is, which in turn offsets the external electric field and weakens the total electric field at the streamer head. According to Figs. 5 and 6, we can conclude that the increasing accumulated surface charge contributes to reducing the propagation velocity of the streamer front in the axial direction.

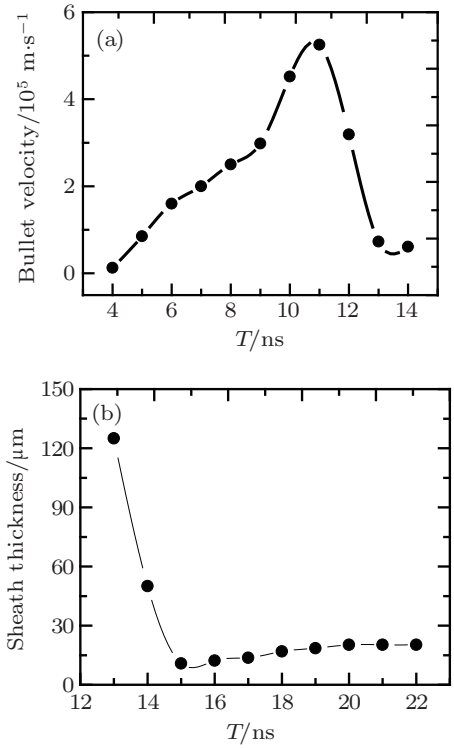


Fig. 5. (a) Axial velocity of the streamer front as a function of time in the first 14 ns, (b) temporal variation of cathode sheath thickness at $r = 0$ mm radial position.

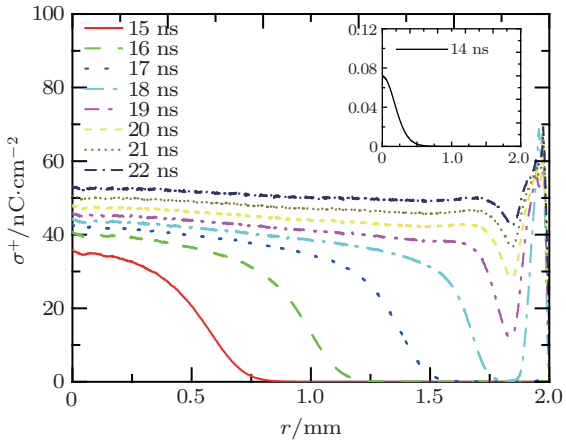


Fig. 6. (color online) Temporal evolutions of the radial distribution of surface charge density on the treated surface.

Although the plasma channel is electrically neutral, it is meaningful to analyze the density distributions of different active particles. For the helium species, the peak density of He* is over 10^{21} m^{-3} and mainly concentrates near the needle tip. Since He* is quickly converted into He_2^* by metastable conversion reaction (R8 in Table 3), the density of He_2^* follows a similar spatial profile to He* (Figs. 7(a) and 7(d)). He^+ is the dominant species near the needle tip and the streamer head as

shown in Fig. 7(b). For the oxygen species, O, O_2^+, and O (1d) almost have the same distribution profiles, which concentrate near the needle tip and in the off-axis region away from the sheath (1.0 mm$< r <$ 1.5 mm, $z = 0.5$ mm). The off-axis peaks in O and O (1d) densities are 6×10^{19} m^{-3} and 4.5×10^{19} m^{-3} respectively, which are higher than the off-axis peak in O_2^+ density and are the key reason for the needle plasma reactivity (see Figs. 7(c), 7(e), and 7(f)). Near the treated surface regions, the ring-shaped density distributions of O and O (1d) suggest the properly treated position of the object for applications. The ambient oxygen diffusion from the surroundings is responsible for these off-axis peaks in O, O_2^+, and O (1d) density. As shown below, the penning ionizations by helium metastables and oxygen from ambient take place in this region, accounting for the off-axis peak in the O_2^+ density.

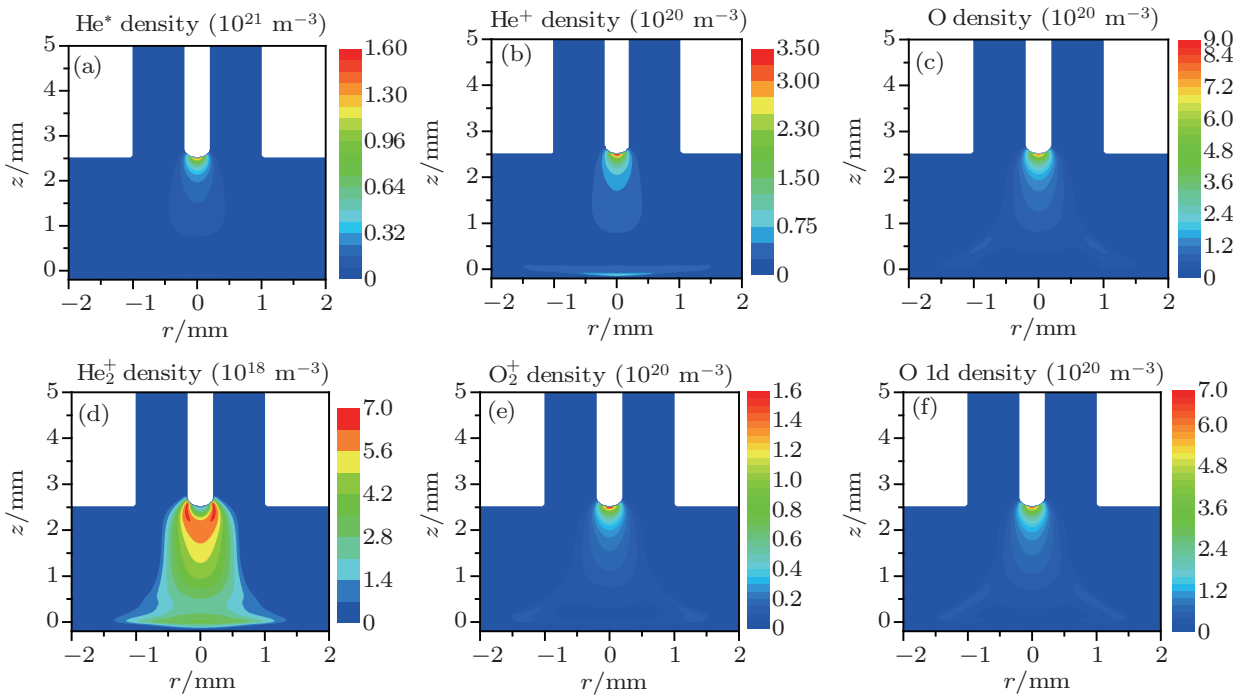


Fig. 7. (color online) Density profiles of needle plasma species at 14 ns.

3.3. Ring-shaped emission profile

In order to understand the different distributions of positive ions, we examine the role of reactions in streamer propagation. Figure 8 shows the profile of ionization reactions of each species. The electron impact ionizations of He and He* concentrate in the streamer head as shown in Fig. 8(a) (R3, R4, and R5), and the peak ionization rate occurs on axis and gradually decreases away from the axis. Their ionization rate is much higher than those of the other cases, thus, He^+ dominates in the ion species in the streamer head. Furthermore, the peak electron ionization rate of O_2 (R28) is only about 6.8% of that of He (Figs. 8(a) and 8(b)). On the other hand, figure 8(c) suggests that the Penning ionization rates of O_2 by He* and He_2^* (R36 and R37) decrease slowly along the channel behind the streamer head. This is attributed to the long lifetimes and high densities of He* and He_2^*. It is important to note that the off-axis peak in Penning ionization rate of O_2 is located at about 1.4 mm away from the axis and about 0.2 mm above the treated surface (see Fig. 8(d)). This peak emission rate is five times higher than the rate on the axis of symmetry at $z = 0.2$ mm. The off-axis emission peak corresponds to the ring-shaped emission profile in our case.

Again, ambient oxygen backdiffusion against the source gas convection is responsible for this interesting emission profile. Figures 9(a) and 9(b) show the contributions of three different reaction mechanisms to the total emission rate at $z = 0.5$ mm and $z = 1.2$ mm respectively as a function of the radial position. The plot clearly shows that the Penning ionization is a dominant reaction, having a peak at $r = 1.1$ mm. However, as shown in Fig. 9(b), the peak values of three different reaction rates are located on the axis and gradually decrease away from the axis. Figure 10(d) further supports our hypothesis. As can be seen, the densities of He* and He_2^* peak on the axis of symmetry and gradually decrease away from the axis. On the other hand, the density of O_2 rapidly and monotonically increases in the radial position. Therefore, the peak in the Penning ionization rate is located at the position where the radially reducing He* and He_2^* distributions cross the radially increasing O_2 profile. Furthermore, the Penning ionization rate profile coincides precisely with the O_2^+ density profile (see Figs. 7(e) and 8(d)), which is due to the fact that Penning ionization is a dominant path to creating O_2^+.

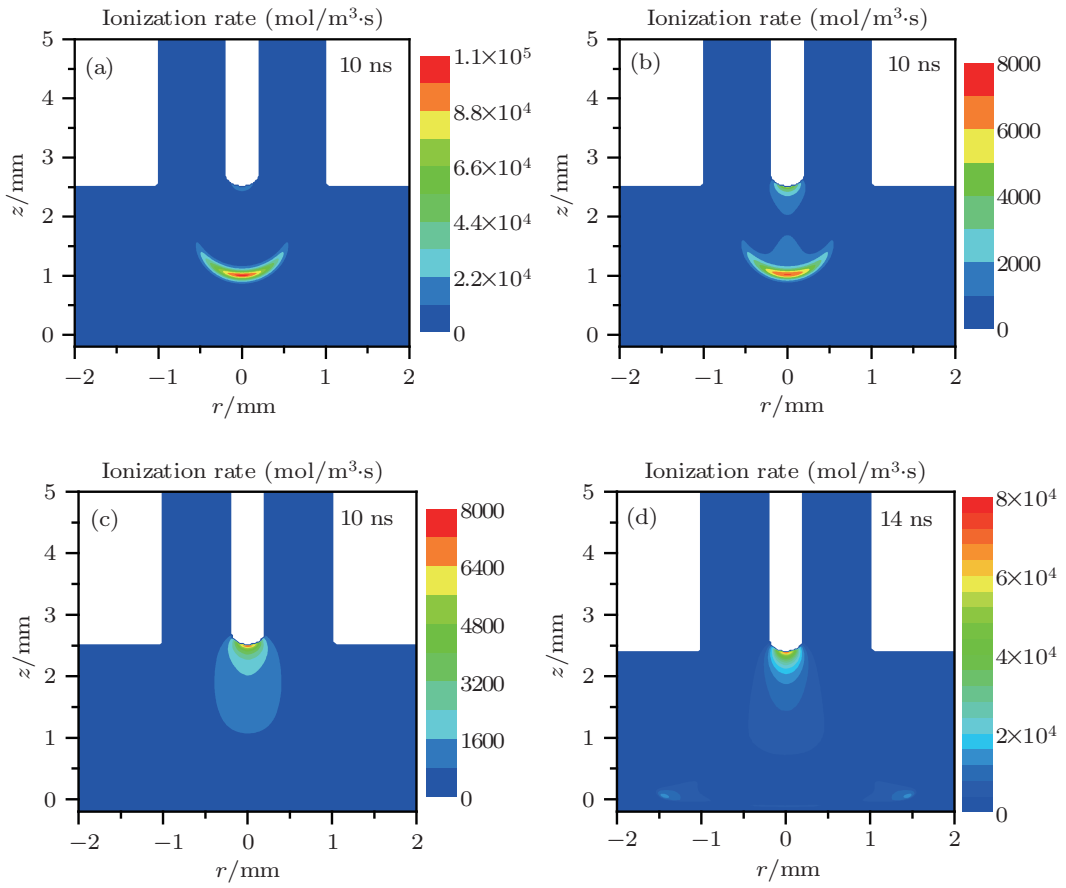


Fig. 8. (color online) Ionization reaction rate (mol/m^3·s) distributions of three different reaction mechanisms. (a) Helium related (R3, R4, and R5), (b) ionization of O_2 by electron (R28), and Penning ionization of O_2 by helium metastables (R36, R37).

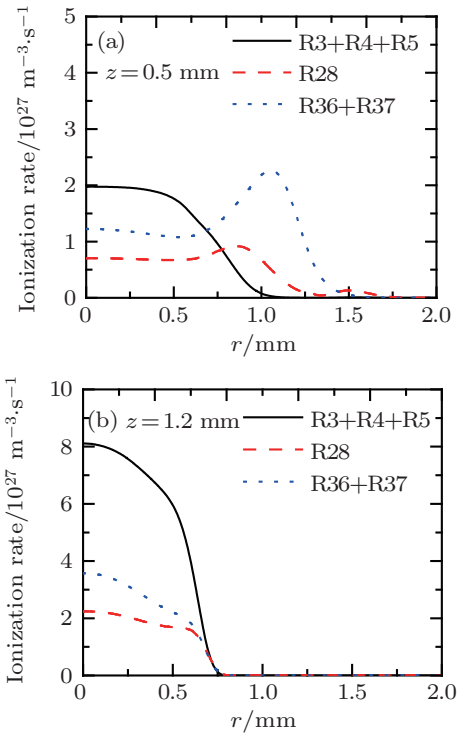


Fig. 9. (color online) Radial profiles of three different reaction rates at (a) $z = 0.5$ mm, and (b) $z = 1.2$ mm.

As discussed above, Goree *et al.*[8,9] reported that the killing pattern of *Streptococcus mutans* bacteria varied from a circle to an annular ring, depending on the input power, as the feed gas flow rate is increased. Furthermore, Sakiyama *et al.*[12] used the TALIF spectroscopy to measure ground atomic oxygen density near a treated surface in needle plasma at atmospheric pressure. According to their experimental results, a circular density distribution was observed at 0.5 SLM, whereas the profile turned into a ring at 1.0 SLM. In this case, we plot the density profiles of O, O (1d), and O_2^+ as a function of radial position at $z = 0.5$ mm in Figs. 10(a)–10(c). As can be seen, the ground atomic oxygen shows a ring-shaped distribution at 1.1 SLM in our work. And the simulated ground atomic oxygen density is on the order of 10^{19} m^{-3}, which is one order of magnitude lower than that measured by TALIF. It should be noted that our model geometry is not identical to their experimental setup due to computational limitations. The mean gas velocity in our model is estimated to be about 6 m/s, which is slightly larger than that in their experiment (3.6 m/s). Furthermore, it is important to note that the RF needle discharge mechanism is quite different from our dc plasma needle. However, both experimental and simulation results show a similar ring-shaped atomic oxygen density profile, which further demonstrates that the simulation results in our model are reasonable.

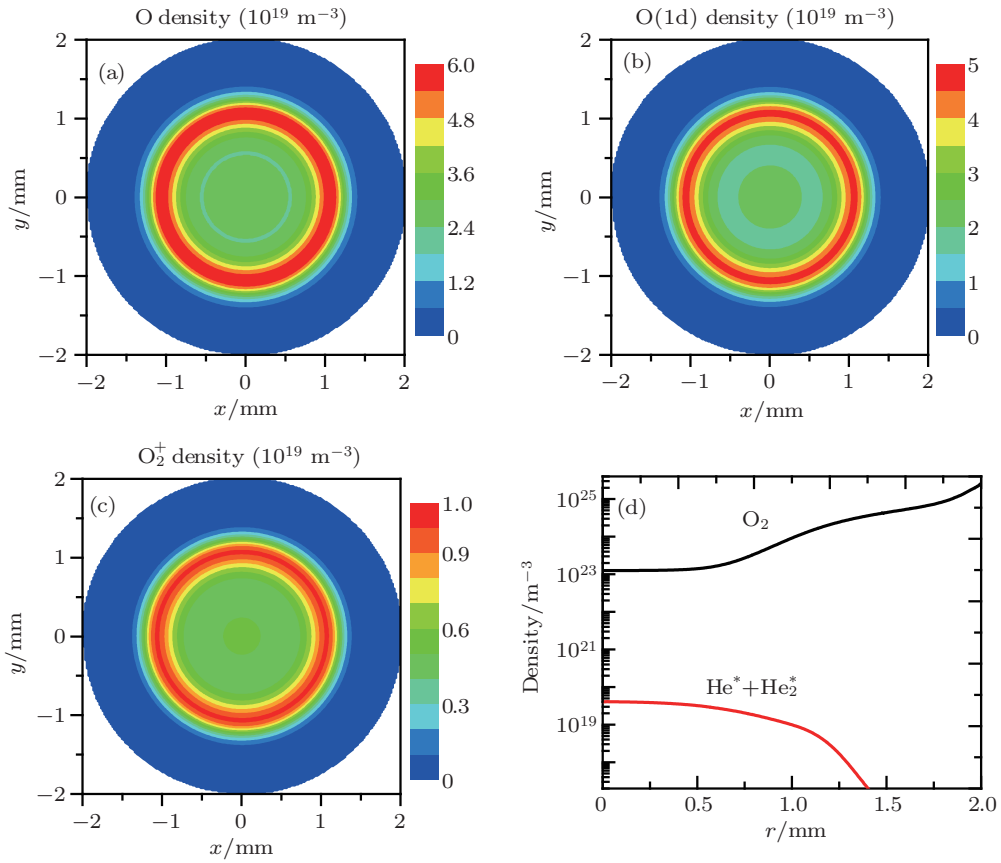


Fig. 10. (color online) Density distributions of (a) O, (b) O (1d), and (c) O_2^+ at $z = 0.5$ mm position, (d) radial distributions of O_2 and the sum of helium metastables at $z = 0.5$ mm.

4. Conclusions

Simulated results of a two-dimensional model coupling neutral gas and plasma dynamics for He/O_2 atmospheric pressure plasma needle discharge are presented in this paper. As a first step of study, only the effect of O_2 in ambient gas is taken into account in this model. The ambient O_2 diffusion from the surroundings is responsible for a peak in the Penning ionization rate at a point off the radial axial, where the radially decreasing He^* and He_2^* distributions cross the radially increasing O_2 profile. In this case, our model reproduces the ring-shaped ground atomic oxygen density profile that appears to be qualitatively similar to that measured by TALIF. The axial propagation velocity of the streamer front is found to be in a range of 10^4 /ms–10^5 m/s. Besides, as the streamer reaches the boundary of the cathode sheath, the increasing accumulated surface charges contribute to stopping the propagation of the streamer front in the axial direction.

References

[1] Fridman G, Friedman G, Gutsol A, Shekhter A B, Vasilets V N and Fridman A 2008 *Plasma Process. Polym.* **5** 503
[2] Kong M G, Kroesen G, Morfill G, Nosenko T, Shimizu T, Dijk J V and Zimmermann J L 2009 *New J. Phys.* **11** 115012
[3] Cheng C, Shen J, Xiao D Z, Xie H B, Lan Y, Fang S D, Meng Y D and Chu P K 2014 *Chin. Phys. B* **23** 075204
[4] Zhou Z Y, Chen G C, Tang W Z and Lü F X 2006 *Chin. Phys.* **15** 980
[5] Stoffels E, Flikweert A J, Stoffels W W and Kroesen G M W 2002 *Plasma Sources Sci. Technol.* **11** 383
[6] Stoffels E, Kieft I E, Sladek R E J, van den Bedem L J M, van der Laan E P and Steinbuch M 2006 *Plasma Sources Sci. Technol.* **15** S169
[7] Kelly S and Turner M M 2011 *J. Appl. Phys.* **110** 053303
[8] Goree J, Liu B, Drake D and Stoffels E 2006 *IEEE Trans. Plasma Sci.* **34** 1317
[9] Goree J, Liu B and Drake D 2006 *J. Phys. D: Appl. Phys.* **39** 3479
[10] Sakiyama Y and Graves D B 2009 *Plasma Sources Sci. Technol.* **18** 025022
[11] Zhang Q, Liang Y D, Feng H Q, Ma R N, Tian Y, Zhang J and Fang J 2013 *Appl. Phys. Lett.* **102** 203701
[12] Sakiyama Y, Knake N, Schröder D, Winter J, der Gathen V S and Graves D B 2010 *Appl. Phys. Lett.* **97** 151501
[13] Yan W, Liu F C, Sang C F and Wang DZ 2015 *Chin. Phys. B* **24** 065203
[14] Naidis G V 2014 *Plasma Sources Sci. Technol.* **23** 065014
[15] Chang Z S, Jiang N, G. Zhang J and Cao Z X 2014 *J. Appl. Phys.* **115** 103301
[16] Hagelaar G J M and Pitchford L C 2005 *Plasma Sources Sci. Technol.* **14** 722
[17] Liu X Y, Pei X K, Lu X P and Liu D W 2014 *Plasma Sources Sci. Technol.* **23** 035007
[18] Breden D, Miki K and Raja L L 2012 *Plasma Sources Sci. Technol.* **21** 034011
[19] Yan W, Liu F C, Sang C F and Wang D Z 2014 *Phys. Plasmas* **21** 013504
[20] Boeuf J P, Yang L L and Pitchford L C 2013 *J. Phys. D: Appl. Phys.* **46** 015201
[21] Walsh J L, Shi J J and Kong M G 2006 *Appl. Phys. Lett.* **88** 171501
[22] Lu X, Naidis G V, Laroussi M and Ostrikov K 2014 *Phys. Rep.* **540** 123
[23] Wu S, Lu X and Pan Y 2014 *Phys. Plasmas* **21** 073509